

ARTICLE OPEN



Effect of exchange-correlation functionals on the estimation of migration barriers in battery materials

Reshma Devi¹, Baltej Singh², Pieremanuele Canepa^{1,2,3✉} and Gopalakrishnan Sai Gautam^{1✉}

Facile ionic mobility within host frameworks is crucial to the design of high-energy-density batteries with high-power-densities, where the migration barrier (E_m) is the governing factor. Here, we assess the accuracy and computational performance of generalized gradient approximation (GGA), the strongly constrained and appropriately normed (SCAN), and their Hubbard U corrections, GGA+ U and SCAN+ U , within the density functional theory-nudged elastic band framework, in the prediction of E_m as benchmarked against experimental data. Importantly, we observe SCAN to be more accurate than other frameworks, on average, albeit with higher computational costs and convergence difficulties, while GGA is a feasible choice for “quick” and “qualitative” E_m predictions. Further, we quantify the sensitivity of E_m with adding uniform background charge and/or the climbing image approximation in solid electrolytes, and the Hubbard U correction in electrodes. Our findings will improve the quality of E_m predictions which will enable identifying better materials for energy storage applications.

npj Computational Materials (2022)8:160; <https://doi.org/10.1038/s41524-022-00837-0>

INTRODUCTION

Rechargeable lithium-ion batteries (LIBs) have been a breakthrough solution for many energy storage applications. However, we have reached a fundamental limit of what we can achieve with the existing LIB technology^{1,2}, with further advancements demanding high-energy density, improved safety, and reduced costs, while maintaining a high rate performance. For instance, the current target of the US Advanced Battery Consortium for batteries used in electric vehicles is to achieve an 80% state-of-charge in 15 min^{3,4}. Recent advancements in using lithium metal anodes, along with compatible solid-state electrolytes can achieve energy densities significantly beyond current LIBs, but poor charging rates (coupled with growth of lithium dendrites) hamper their performance⁵. Multivalent (MV) batteries^{6–8}, such as those involving Mg ions, provide an alternative to LIBs in offering systems with higher volumetric energy densities (due to the use of a metallic anode^{9–11}), but also suffer from poor rate performance^{7,12}. Thus, it becomes essential to understand and improve rate performance in batteries, where computational tools can play a key role.

A critical factor that influences the rate performance of batteries is the diffusion of the electroactive ions in the active materials (i.e., solid electrodes and/or electrolytes), which in turn is largely influenced by the ionic migration barriers (E_m) within host frameworks¹³. The conventional theoretical methodology to estimate E_m is using the computationally intensive density functional theory^{14,15} (DFT)-based nudged elastic band¹⁶ (NEB) calculations and/or ab initio molecular dynamics (AIMD) simulations^{17,18}. Our work focuses on DFT-NEB calculations, which usually is the preferred mode of estimating E_m , especially in frameworks with “high” barriers¹⁹. This is because the accuracy of AIMD calculations depends on the robust sampling of migration events¹⁷, which can be difficult in events with low jump frequencies (caused by high E_m). Note that the central approximation in performing either DFT-NEB or AIMD calculations is the

choice of the exchange-correlation (XC) functional, which broadly describes the nature of bonding and the quantum mechanical interactions among the electrons present in a system.

A popular choice of XC functional (for DFT-NEB and AIMD) is the Perdew–Burke–Ernzerhof²⁰ (PBE) generalized gradient approximation (GGA), due to its reasonable trade-off between computational cost and accuracy^{21–24}. However, PBE suffers from several shortcomings, such as self-interaction errors (SIE) in transition-metal (TM) systems^{25,26}, overbinding of the oxygen gas molecule^{27–29}, and the inability to account for van der Waals interactions associated with layered frameworks^{30–32}. Several modifications have been made to improve upon PBE to capture specific ground state properties of interest, resulting in functionals, such as PBEsol³³, PBEfe³⁴, and AM05³⁵, but none have fully replaced PBE. Another approach to mitigate inaccuracies incurred within the general class of GGA functionals (including PBE) is to employ a meta-GGA framework, such as the Minnesota³⁶ or the strongly constrained and appropriately normed (SCAN^{37,38}) functional. Importantly, the SCAN functional satisfies all the 17 known constraints of an XC functional (PBE does not satisfy)³⁹, does not overbind oxygen molecule⁴⁰, accurately predicts formation enthalpies of main group compounds⁴¹, estimates the ground state structural and electronic properties better (than GGA)⁴², and usually predicts the correct ground state polymorph in compositions where multiple polymorphs can exist⁴³. As SCAN has been developed recently, it has not been widely benchmarked and used to calculate E_m , yet, in solids. Thus, one of the aims of this article is to test the accuracy of SCAN in E_m predictions in materials for energy storage.

In the case of TM-containing oxide frameworks, both PBE and SCAN exhibit significant SIEs^{26,40,44,45}. One of the techniques used to reduce the SIE, in both PBE and SCAN, is to introduce an empirical Hubbard U parameter⁴⁶, resulting in a PBE+ U ^{44,47} (or equivalently GGA+ U) and SCAN+ U ⁴⁰ functional, respectively. While the computational cost for a GGA+ U or SCAN+ U is similar

¹Department of Materials Engineering, Indian Institute of Science, Bengaluru, Karnataka, India. ²Department of Materials Science and Engineering, National University of Singapore, Singapore, Singapore. ³Department of Chemical and Biomolecular Engineering, National University of Singapore, Singapore, Singapore. ✉email: pcanepa@nus.edu.sg; saigautam@iisc.ac.in

to the corresponding GGA or SCAN calculation, GGA+ U /SCAN+ U is better at predicting the electronic and redox properties of TM-containing compounds compared to GGA/SCAN^{40,44,48,49}. Nevertheless, the Hubbard U -corrected functionals are not widely used for estimating E_m in solids, primarily because of convergence difficulties in performing NEB calculations^{50,51}. Additionally, U -corrected functionals are expected to overestimate E_m , particularly in electrode frameworks that form polarons^{52–54} within the bulk structure. This is because the migration of a cation in such structures involves the migration of a localized electron, creating configurations with partial electronic occupancies across different TM sites, especially “near” the transition state (TS). Such partially occupied states are penalized by the Hubbard U framework, resulting in an underestimation of the TS energy and an overestimation of E_m . Nevertheless, a robust evaluation of the computational performance and accuracy of GGA and SCAN and their corresponding U -corrected versions is required before any specific computational framework can be employed in a more widespread manner.

To date, studies have focused on understanding the influence of XC frameworks, especially with SCAN, on several “static” properties, such as intercalation voltages^{55–58}, band gaps⁵⁵, interlayer spacings⁵⁵, and magnetic properties⁵⁷, and not on “dynamic” properties such as E_m . In this study, we perform a detailed investigation of the impact of the XC functional choice on E_m predictions in six different well-studied electrodes, namely the layered-LiCoO₂ (space group: $R\bar{3}mH$), the spinels-LiMn₂O₄ ($Fd\bar{3}m$), MgMn₂O₄ ($I4_1/amd$), and Mg_xTi₂S₄ ($Fd\bar{3}m$), the olivine-LiFePO₄ ($Pnma$), and the post-spinel-NaV₂O₄ ($Pnma$). Also, we consider three different solid electrolytes, namely the spinel-MgSc₂Se₄ ($Fd\bar{3}m$), the tetragonal-Na₃PS₄ ($P\bar{4}2_1c$), and the orthorhombic-Li₃PO₄ ($Pnma$). The choice of materials studied in this work are motivated by: (i) the availability of experimental mobility data, (ii) the diversity of structural frameworks (layered, spinel, post-spinel, etc.) with different redox-active TMs (such as, Co, Mn, Fe, V, Mn, and Ti), and (iii) the heterogeneity of intercalant (or mobile) cations, including Li⁺, Na⁺, and Mg²⁺.

We consider four different XC functionals for calculating E_m in electrode materials: GGA (PBE), SCAN, GGA+ U , and SCAN+ U . While a number of strategies have been proposed in determining U values⁵⁹, we employ U corrections, with both GGA+ U and SCAN+ U , that are optimized to reduce errors against experimental oxidation enthalpies^{40,44,45,60}. This choice is ideal since ionic migration in electrodes often involves a “local” redox process, with the migrating ion typically causing the movement of electron(s) as well^{50,61}. Furthermore, modeling ionic migration via vacancy-mediated-hops results in the presence of mixed TM oxidation states, which are best described with an “averaged” U parameter. Apart from the XC functionals considered, we have also analyze the role of adding a uniform background charge (UBC) and using the climbing image (CI¹⁶) approximation on calculated E_m in the solid electrolytes considered (see Migration barriers section under Results).

The main objective of our work is to validate the calculated E_m with the various XC approximations with existing experimental data for the nine prototype materials mentioned above. Overall, we observe that SCAN provides a marginally better quantitative accuracy of E_m across all materials considered on average, compared to GGA and the U -corrected frameworks, albeit with several exceptions. In solid electrolytes, we do not find the addition of a UBC and/or the CI framework to significantly alter E_m with both GGA and SCAN, except for Li₃PO₄. Importantly, E_m evaluated with SCAN are larger than those with GGA across several materials, which leads to SCAN (GGA) providing a qualitative upper (lower) bound to the experimental E_m . Furthermore, the addition of U corrections (in electrodes) has a lower impact on SCAN- E_m than GGA, which can be attributed to the better description of the underlying electronic structure, as

characterized by the on-site magnetic moments on TMs. Therefore, among the XC functionals considered here, we expect SCAN to be the best choice of XC framework for E_m predictions, although with higher computational costs and convergence difficulties than GGA-based functionals. Also, we note that GGA can provide better E_m estimates than SCAN in specific materials, such as Mg_xTi₂S₄, MgSc₂Se₄, and Li₃PO₄, thus making E_m evaluations with GGA quite useful. Our work provides a better understanding of the underlying physics behind the estimation of E_m s in energy storage materials, and will aid in the selection of the right XC functional for a given structure in future studies, thus enabling the discovery of ion conducting electrodes and solid electrolytes via computational workflows⁶².

RESULTS

Structures

Figure 1 shows the structures of the materials considered in this work, with additional details reported in Supplementary Table 1 of the electronic supporting information (ESI). Li₃PO₄, which is a solid electrolyte with high Li-conductivity and ease of preparation⁶³ can be experimentally synthesized in two different phases, γ and β ⁶⁴. The γ -Li₃PO₄ polymorph ($Pnma$ space group, Fig. 1a) exhibits oxygen atoms arranged in a hexagonal-close-packed sub-lattice, with Li and P atoms occupying 16 out of 32 available tetrahedral voids. We consider the γ polymorph instead of β since it is an ordered configuration of Li₃PO₄ despite being thermodynamically metastable⁶⁵. Similar to Li₃PO₄, the Na ionic conductor, Na₃PS₄ also exhibits one of two polymorphs, the tetragonal-Na₃PS₄ (or t-Na₃PS₄, $P\bar{4}2_1c$, (Fig. 1b)) and the cubic-Na₃PS₄ (or c-Na₃PS₄, $\bar{I}43m$), at 298 K, depending on the synthesis technique^{66–68}. The main difference between the two structures of Na₃PS₄ is the split of the Na(6b) site in the cubic phase into two sites, Na1(2a) and Na2(4d) in the tetragonal phase^{67,68}, as indicated in Fig. 1b. We investigate the t-Na₃PS₄ as it is stable and exhibits an ordered structure⁶⁹.

Figure 1d displays the O3 phase⁷⁰, an important ordering of Li_xCoO₂, which exhibits oxygens in a “ABCABC”-type stacked close-packed layers with the Li and Co positioned in octahedral sites across alternate cation layers⁷¹. We consider the so-called divacancy (DV⁷²) hop for estimating the E_m in Li_xCoO₂, while the calculated E_m for the monovacancy hop is included in Supplementary Fig. 1 of the ESI. Another commercial electrode material for LIBs is LiFePO₄ (Fig. 1h) that exhibits an ordered olivine-type structure ($Pnma$), consisting of corner-sharing FeO₆ octahedra and PO₄ tetrahedra with the Li ions residing in “tunnels” along the b -axis. Both LiCoO₂ and LiFePO₄ are well-studied Li-ion cathode frameworks^{73,74}. The Na-cathode considered in this work is the post-spinel NaV₂O₄ ($Pnma$, Fig. 1e), where the mobile Na ions are located in the center of 1D tunnels formed by the edge sharing VO₆ octahedra, along the b axis.

Among the four spinels considered here, the MgMn₂O₄ (Fig. 1g, $I4_1/amd$) is one of the Mg oxide-cathodes to exhibit a reasonable extent of Mg mobility^{75,76}. MgMn₂O₄ adopts either a tetragonal or cubic symmetry depending on the concentration of Jahn-Teller distorted Mn³⁺, which is determined by both the Mg content and the degree of spinel “inversion”⁷⁵. Ideally, for $x_{Mg} = 1$, the structure of MgMn₂O₄ is tetragonal. On the other hand, spinels-MgSc₂Se₄ and LiMn₂O₄ (Fig. 1f) are cubic ($Fd\bar{3}m$) since they have cations that do not exhibit cooperative Jahn-Teller distortion. In the case of spinel-Mg_xTi₂S₄ (Fig. 1c), the intercalated Mg atoms occupy octahedral sites within the cubic structure instead of the typically occupied tetrahedral positions⁷⁷. Note that we have calculated the E_m for Mg_xTi₂S₄ in the high-vacancy limit (i.e., $x \rightarrow 0$), since the Mg sub-lattice is disordered at high Mg concentrations (at $x \rightarrow 1$). For all electrodes except Mg_xTi₂S₄, we have calculated the E_m at the dilute-vacancy limit (see Methods section).

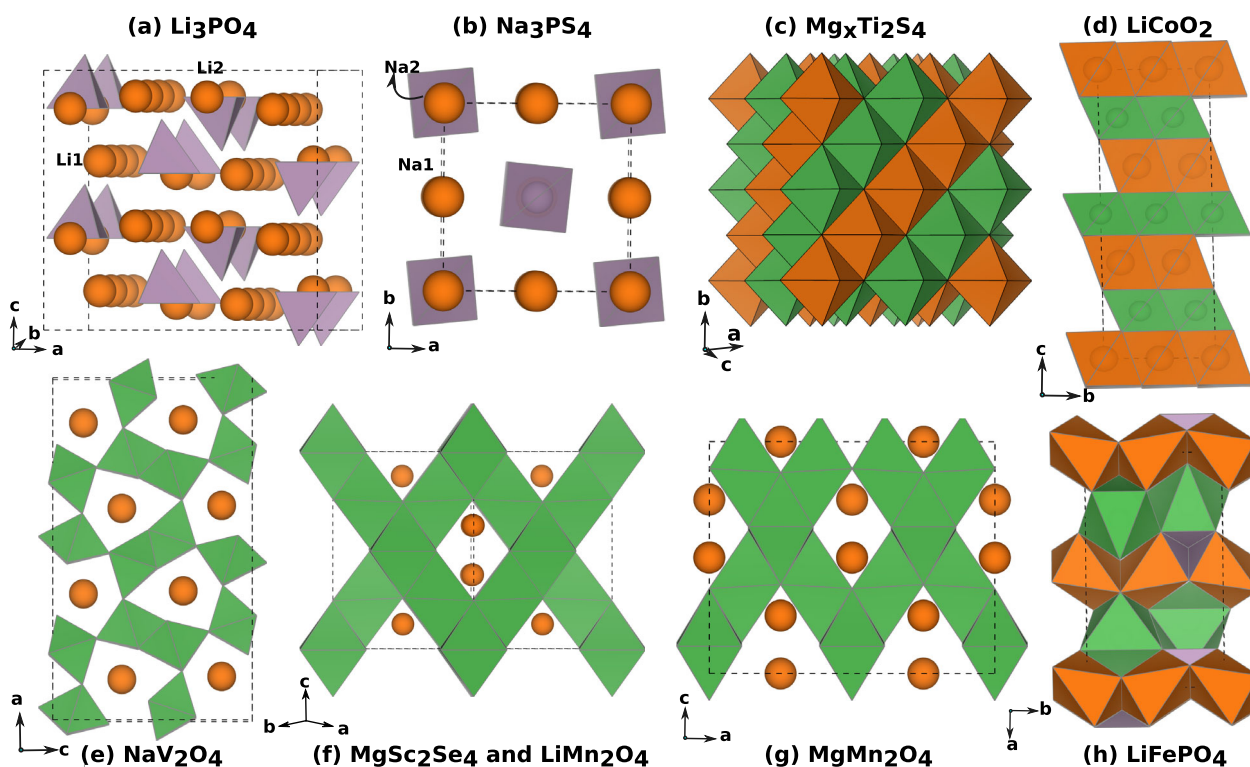


Fig. 1 Supercells of all the structures considered in this work. The migrating and the transition-metal ions are represented by orange and green spheres/polyhedra respectively. Phosphate ions are shown by purple polyhedra.

Migration barriers

We compare barriers obtained from the various XC frameworks (colored bars) against experimental data^{76–84} (horizontal dashed lines) of electrodes and solid electrolytes in the top and bottom panels of Fig. 2. The detail on synthesis and measurements of ionic mobility employed experimentally for all materials are listed in Supplementary Table 2 of the ESI. Numerical values of E_m are listed in Table 1. Minimum energy pathways (MEPs) and E_m not included in the main text are compiled in the ESI (Supplementary Figs. 1–8). In solid electrolytes, we do not consider the U -corrected functionals since these materials do not contain redox-active TMs with partially filled d orbitals⁸⁵. Note that ionic migration in solid electrolytes considered here occurs via the vacancy-mediated mechanism, which requires the creation of a Li/Na/Mg vacancy within the stoichiometric supercell used in the NEB calculation. Subsequently, a UBC is often added to the periodic cell (referred to in this work as “NELECT”)^{86,87} to maintain charge neutrality during the calculation. Since the impact of adding a UBC on E_m has not been rigorously quantified in diverse solid electrolytes before, we have calculated E_m using both GGA and SCAN XC with and without NELECT. Note that interstitial/interstitialcy-based migration mechanisms can be active in solid electrolytes, particularly in disordered systems⁸⁸, but not considered in this work.

The CI framework involves a modification to the regular NEB in removing the spring forces surrounding the image with the highest energy, nominally allowing for a better description of the TS (i.e., the saddle point)¹⁶. While CI-NEB has been shown to more accurately predict E_m , it can be computationally difficult to converge⁸⁹. Hence, for NEB calculations in solid electrolytes, we also perform a CI-NEB calculation for each XC framework considered, after the regular NEB converged, to estimate any changes in the calculated E_m .

An examination of the data suggests that the magnitude of E_m predicted by SCAN is higher compared to GGA, while the barriers

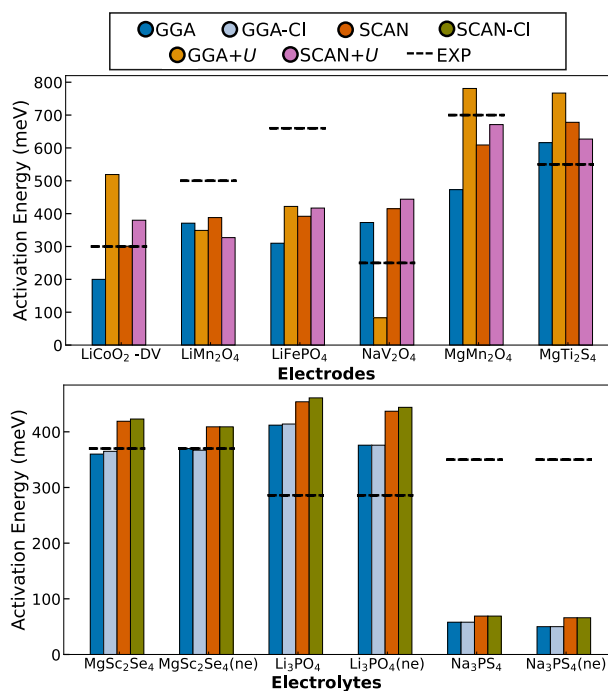


Fig. 2 Computed barriers, using different XC frameworks, for the electrodes (top panel) and solid electrolytes (bottom panel) considered in this work. Horizontal dashed lines indicate experimentally reported values. “ne” in the electrolytes panel indicates the inclusion of UBC (i.e., NELECT) in the NEB calculation, while bars corresponding to “CI” highlight the usage of the climbing image framework. Barriers plotted for Li_3PO_4 are for the 1(d) \rightarrow 2(c) hop. “DV” in LiCoO_2 -DV stands for the divacancy hop mechanism.

Table 1. Experimental and computed migration barriers E_m (in meV) of all materials considered in this work.

Electrodes	Migration path ^a	E_m				
		Exp.	GGA	GGA+ <i>U</i>	SCAN	SCAN+ <i>U</i>
Layered LiCoO ₂ (divacancy hop) <i>R3mH</i>	oct → tet → oct	300 ⁷⁸	200	519	301	380
Spinel-LiMn ₂ O ₄ <i>Fd3m</i>	tet → oct → tet	500 ± 100 ⁷⁹	371	349	388	327
Olivine-LiFePO ₄ <i>Pnma</i>	Along <i>b</i> axis	660 ⁸⁰	310	422	392	417
Post-spinel-NaV ₂ O ₄ <i>Pnma</i>	Along <i>b</i> axis	225 ⁸¹	373	83	415	444
Spinel-MgMn ₂ O ₄ <i>I4₁/amd</i>	tet → oct → tet	700 ± 60 ⁷⁶	473	781	609	671
Spinel-Mg _x Ti ₂ S ₄ <i>Fd3m</i>	oct → tet → oct	500 ⁷⁷	616	767	678	627
Electrolytes		Exp.	GGA	GGA + NELECT	SCAN	SCAN + NELECT
Spinel-MgSc ₂ Se ₄ <i>Fd3m</i>	tet → oct → tet	370 ± 90 ⁸²	360	370	419	409
Spinel-MgSc ₂ Se ₄ (with Cl) <i>Fd3m</i>	tet → oct → tet	370 ± 90 ⁸²	365	367	423	409
Tetragonal-Na ₃ PS ₄ <i>P4₂1c</i>	Along <i>a</i> axis	350 ⁸³	58	50	69	66
Tetragonal-Na ₃ PS ₄ (with Cl) <i>P4₂1c</i>	Along <i>a</i> axis	350 ⁸³	58	50	69	66
Orthorhombic-Li ₃ PO ₄ <i>Pnma</i>	1(<i>d</i>) → 2(<i>c</i>)	286 ± 60 ⁸⁴	412	376	454	437
Orthorhombic-Li ₃ PO ₄ (with Cl) <i>Pnma</i>	1(<i>d</i>) → 2(<i>c</i>)	286 ± 60 ⁸⁴	414	376	461	444
Orthorhombic-Li ₃ PO ₄ <i>Pnma</i>	2(<i>c</i>) → 3(<i>d</i>)	–	713	735	721	739
Orthorhombic-Li ₃ PO ₄ (with Cl) <i>Pnma</i>	2(<i>c</i>) → 3(<i>d</i>)	–	713	735	721	739
Orthorhombic-Li ₃ PO ₄ <i>Pnma</i>	1(<i>d</i>) → 2(<i>c</i>) → 3(<i>d</i>)	–	605	821	669	824
Orthorhombic-Li ₃ PO ₄ <i>Pnma</i>	1(<i>d</i>) → 2(<i>c</i>) → 3(<i>d</i>)	–	705	879	727	877

^aThe migration path column indicates the specific ionic migration pathway calculated.

reported by SCAN+*U* are lower than GGA+*U* in electrodes (with NaV₂O₄ being the only exception). In solid electrolytes, the addition of NELECT does not impact the GGA or the SCAN barriers as seen in MgSc₂Se₄ and Na₃PS₄. In contrast, adding NELECT does affect the barriers of Li₃PO₄, by ~9% for GGA and ~4% for SCAN (for the 1(*d*) → 2(*c*) hop, see Li₃PO₄ section for additional details). In general, adding NELECT reduces E_m marginally. The addition of Cl in our calculations does not change the barrier for a given functional (except in the case of Li₃PO₄), with variations of $E_m < 2\%$ across all corresponding XC functionals, with and without Cl.

Overall, the barriers predicted by SCAN have a better numerical accuracy compared to GGA or the Hubbard *U*-corrected frameworks, with a mean absolute error (MAE) of ~140 meV when compared to 178.33, 183, and 145.17 meV for GGA, GGA+*U*, and SCAN+*U*, respectively. There are specific exceptions where GGA performs better than SCAN including NaV₂O₄, Mg_xTi₂S₄, MgSc₂Se₄, and Li₃PO₄. Similarly, in LiFePO₄, LiMn₂O₄, and NaV₂O₄, GGA+*U* exhibits lower errors (MAE ~177 eV) than SCAN+*U* (~212 eV). Further, we discuss in detail systems, including γ -Li₃PO₄, t-Na₃PS₄, spinel-MgMn₂O₄, and layered-LiCoO₂, in the following sections to highlight the general trends and specific anomalies.

γ -Li₃PO₄

Out of the several possible migration paths along the three orthogonal axes of Li₃PO₄, the migration of a Li-vacancy occurs along a zig-zag path across the two nonequivalent Li sites, namely Li1 and Li2, which are also referred to as “*d*” and “*c*” sites, as in Fig. 1a. Specifically, the presence of these two Li sites leads to a 1(*d*) → 2(*c*) → 3(*d*) hop, requiring the presence of two metastable Li vacancies, as shown by the blue spheres in Fig. 3a and the black arrows in its inset. Note that 1(*d*) and 3(*d*) are symmetrically equivalent Li1 sites, but are named so to distinguish them during Li migration, as per the notation by Du and Holzwarth⁹⁰. The energy of formation of a Li vacancy over the *d* and *c* sites, with multiplicity 8 and 4, respectively, differ by ~0.22 eV⁹⁰. There are three Li-hops that can be calculated in Li₃PO₄: (i) 1(*d*) → 2(*c*), (ii) 2(*c*) → 3(*d*), and (iii) 1(*d*) → 2(*c*) → 3(*d*).

Figure 3b, c show the MEPs and the corresponding barriers (in meV) for the 1(*d*) → 2(*c*) hop, without and with NELECT, respectively. The barriers pertaining to the 1(*d*) → 2(*c*) → 3(*d*) divacancy and 2(*c*) → 3(*d*) hops are included in the ESI (Supplementary Fig. 7). In general, E_m predicted by SCAN XC functional in Li₃PO₄ (for all hops considered) are higher than the corresponding

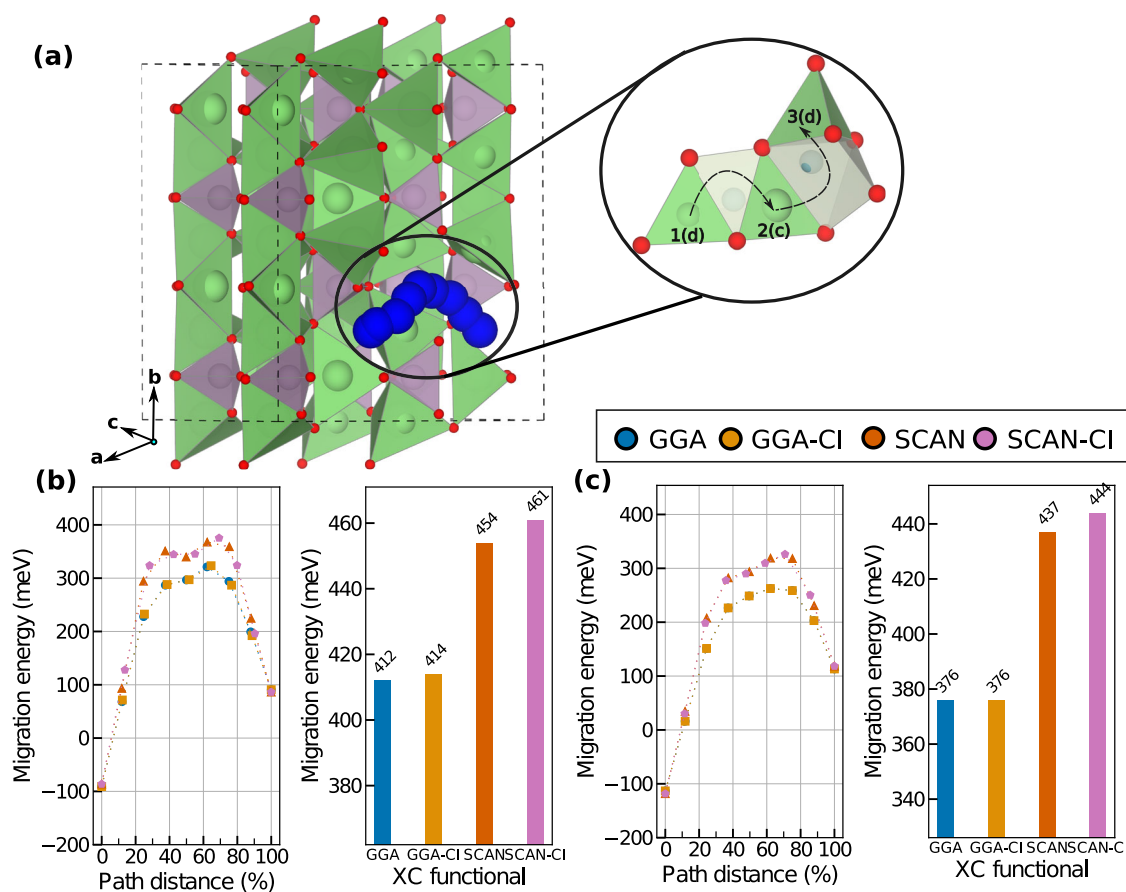


Fig. 3 Migration pathway and computed barriers for γ - Li_3PO_4 . **a** $1 \times 2 \times 2$ supercell of Li_3PO_4 used for the NEB calculations. Green and purple polyhedra represent LiO_6 and PO_4 groups, respectively. The inset shows the migration of the Li ion along the 1(d) \rightarrow 2(c) \rightarrow 3(d) path (blue spheres). **b** MEPs and E_m are plotted for the 1(d) \rightarrow 2(c) pathway, without NELECT. GGA+CI and SCAN+CI indicate CI-NEB calculations with GGA and SCAN, respectively. **c** MEPs and E_m for the 1(d) \rightarrow 2(c) path, with NELECT added.

GGA approximation. The addition of CI does not alter the magnitude of E_m significantly, except in the case of the 1(d) \rightarrow 2(c) \rightarrow 3(d) hop which shows a maximum deviation of $\sim 16\%$ (between GGA and GGA + CI, without NELECT). The qualitative nature of the MEPs captured by both GGA and SCAN XC functionals is similar, and does not change significantly with the inclusion of NELECT. However, adding NELECT does change the magnitude of E_m significantly in some hops of Li_3PO_4 , with the variation higher in GGA-based frameworks (~ 3 – 35% variation from the corresponding E_m without NELECT) than SCAN-based (~ 2 – 23% variation).

The barrier for the 1(d) \rightarrow 2(c) hop is lower than for the 2(c) \rightarrow 3(d) hop, which is consistent with the report by Du and Holzwarth⁹⁰ with our calculated GGA+CI and GGA E_m also exhibiting good agreement (see Supplementary Fig. 7). The E_m for the 1(d) \rightarrow 2(c) \rightarrow 3(d) hop, when considered along with the vacancy formation energy is consistent with the effective activation barrier reported in the impedance spectroscopic study by Ivanov-Shitz et al.⁹¹ The experimentally reported E_m for Li^+ migration in a solid solution of $\text{Li}_{3+x}\text{P}_{1-x}\text{Si}_x\text{O}_4$ ($0 < x < 0.4$) with the γ - Li_3PO_4 structure, via nuclear magnetic resonance (NMR) measurements, is $\sim 27.6 \pm 0.7$ kJ per mol ($\sim 286.05 \pm 6$ meV) for 80 mol% Li_3PO_4 ⁸⁴. The E_m predicted by GGA+NELECT for the 1(d) \rightarrow 2(c) hop is closest to the experimental value (albeit a significant $\sim 31\%$ error) while SCAN+NELECT overestimates it by $\sim 52\%$. The addition of NELECT does improve the numerical accuracy of both GGA and SCAN (for the 1(d) \rightarrow 2(c) hop) with respect to experimental data. Note that our on-site magnetic moment data does not indicate any significant electron

localization upon NELECT addition (with either GGA or SCAN), ruling out any localization of electrons contributing to better E_m agreement with experiments.

Tetragonal- Na_3PS_4

The t- Na_3PS_4 supercell used in our NEB calculation is shown in Fig. 4a, with the blue spheres indicating the migrating Na atom. Orange and yellow spheres represent the Na1 and Na2 sites, respectively. Purple squares represent the PS_4 polyhedra. There are two pathways in which the Na ion can diffuse through the structure: (i) hop from Na2 to Na1 site along with the a or b axis and (ii) hop from Na2 to a neighboring Na2 site along the c axis. We investigate the Na1 \rightarrow Na2 hop (Fig. 4a) since a previous study has reported that the Na2 \rightarrow Na1 hop is more facile than the Na2 \rightarrow Na2 hop⁸³. Also, several experimental studies have been conducted to study the Na ion mobility in Na_3PS_4 . For example, Chu et al.⁹² reported that pristine t- Na_3PS_4 exhibits a conductivity of ~ 0.01 mS/cm at 300 K, corresponding to an E_m of ~ 317 meV, using impedance spectroscopy, while similar measurements by Krauskopf et al.⁹³ and Chang et al.⁸³ reported E_m of ~ 380 and ~ 350 meV, respectively.

Figure 4b shows the calculated MEPs and E_m for the GGA and SCAN functionals, with and without NELECT. The magnitude of E_m is unaltered on including the CI approximation and are only marginally affected by the inclusion of NELECT with both GGA and SCAN (maximum change of ~ 8 meV). The shape of the MEPs are qualitatively similar across all the four XC frameworks. Similar to Li_3PO_4 , SCAN-based calculations predict a higher E_m compared to corresponding GGA-based versions. Moreover, the difference in

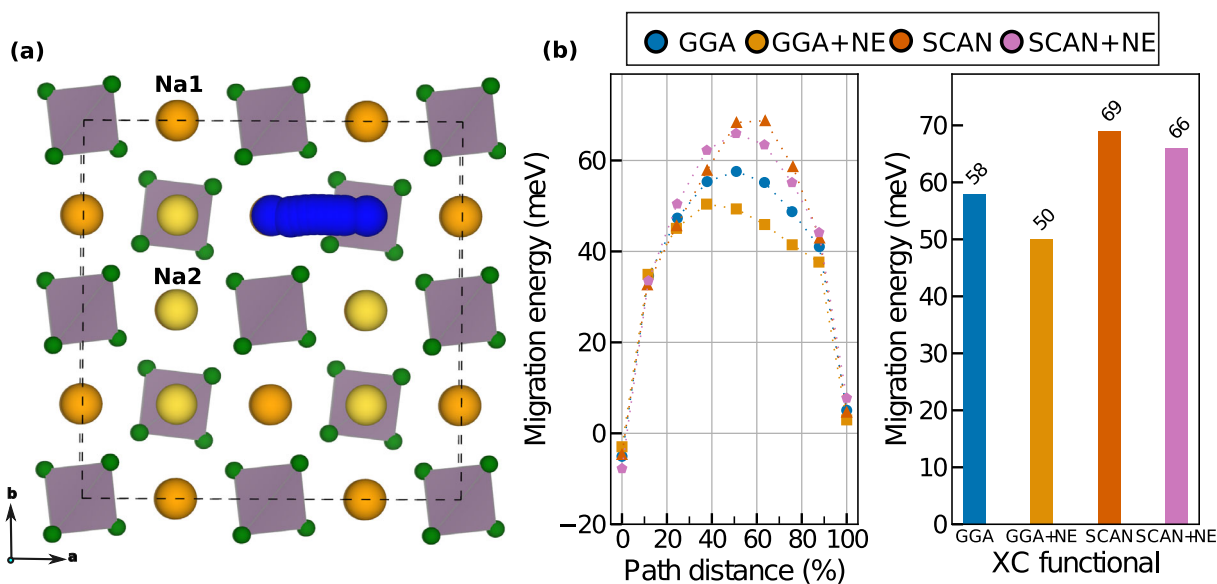


Fig. 4 MEPs and the corresponding barriers for Na₃PS₄. **a** $2 \times 2 \times 2$ supercell of Na₃PS₄. Na1 and Na2 sites are represented by orange and yellow spheres, respectively. Blue spheres indicate the Na migration pathway. **b** MEPs and E_m for the Na1 → Na2 hop. GGA + NE and SCAN + NE indicate calculations with NELECT added.

E_m with NELECT addition in SCAN (~ 3 meV) is lower than in GGA (~ 8 meV), similar to trends observed in Li₃PO₄. However, all our calculated E_m are significantly lower than experimental reports (by ~ 300 meV), while classical MD simulations have predicted barriers in better agreement with experiments⁹⁴.

Note that our calculated E_m are consistent with the GGA- E_m of Huang et al.⁶⁶ and Yu et al.⁹⁵ for the Na2 → Na1 hop, suggesting that the large discrepancy between DFT and experimental activation energy values may be largely attributed to the non-inclusion of defect formation energies in E_m calculated by NEBs. Indeed, previous AIMD simulations^{66,96} have indicated a decrease in E_m (from >300 meV in pristine-Na₃PS₄ to <280 meV) due to the presence halogen dopants (which nominally create Na-vacancies) in both c-Na₃PS₄ and t-Na₃PS₄.

Spinel-MgMn₂O₄

Spinel-MgMn₂O₄ has its oxygen anions adopting a face-centered-cubic lattice, with half of the octahedral voids occupied by Mn and 1/8th of the tetrahedral voids occupied by Mg. Mg²⁺ in MgMn₂O₄ migrate across a $8a \rightarrow 16c \rightarrow 8a$ pathway, where the initial and final $8a$ sites share a triangular face with the intermediate, empty octahedral ($16c$) site. The edges of the $16c$ site are shared by six other Mn octahedra, resulting in a “ring” of Mn sites adjacent to it⁷⁵. Figure 5a provides a closer look of the $16c$ and the adjacent ring sites (solid yellow lines), with the left and right images indicating the view from “top” and “bottom”, respectively. The text annotations on each Mn site in Fig. 5a identify the specific Mn ring site. Green and purple octahedra, respectively, represent the initial and the final $8a$ sites of the migrating Mg ion. The yellow upright (inverted) triangle signifies Mn octahedra coming out (pointing into) the plane of the paper. The inverted triangle represents Mn24 and Mn23 in the left and right subpanel, respectively, while the upright triangle signifies Mn20 in both subpanels. Another view of the Mn sites adjacent to the initial and final $8a$ sites is provided in Supplementary Fig. 9a.

Panel b of Fig. 5 shows the MEPs (left subpanel) and the corresponding E_m as bar charts (right subpanel). Figure 5c shows the on-site magnetic moments of all TM ions (i.e., Mn) in the MgMn₂O₄ structure used for the NEB calculation, as a function of the image number (where each image represents a snapshot of

Mg during its migration). Specifically, image number 1 (9) represents the initial (final) Mg site. The TM number in panel c is identical to the notation used for labeling Mn ions in panel a. The on-site magnetic moments are represented via the heat map ranging from $2.5 \mu_B$ to $4 \mu_B$, where the lower (higher) values represent Mn⁴⁺ (Mn³⁺). Importantly, changes in magnetic moments track the movement of electrons as Mg migrates within the spinel.

Note that due to convergence difficulties, we had to use a different supercell and relaxation scheme for the GGA-NEB calculation of MgMn₂O₄, which explains the different number of TMs for GGA (see Supplementary Fig. 9b). Notably, GGA wrongly predicts the bulk cubic version of spinel-MgMn₂O₄ to be the ground state instead of the tetragonal, Jahn-Teller distorted structure⁹⁷. This is because GGA wrongly delocalizes the valence electrons between Mn and O atoms to an extent that it cannot account appropriately for the Jahn-Teller distortion of Mn³⁺. In contrast, SCAN(+ U) and GGA+ U functionals, with their intrinsic tendency to decrease the SIE, rightly predict the tetragonal polymorph to be the ground state. Therefore, care must be taken to ensure that the “right” structure is used for calculating E_m with GGA in the case of Jahn-Teller distorted structures. To address this issue here, we have used a PBEsol+ U -relaxed spinel conventional cell containing 56 atoms (without Mg vacancy) to initialize the endpoint images and subsequently the NEB calculation, which is identical to the procedure of Gautam et al.⁷⁵.

From Fig. 5b, we observe that the MEPs are qualitatively similar, with all functionals displaying a local energy minimum corresponding to the $16c$ site. Importantly, the E_m calculated with GGA+ U , SCAN, and SCAN+ U tend to be in reasonable agreement with the experimentally reported E_m (700 ± 60 meV)⁷⁶. Specifically, the maximum and minimum error, with respect to experiment, among these XC frameworks is about 13% (SCAN) and 4% (SCAN+ U), respectively. On one hand, the magnitude of error reported experimentally (i.e., a window of 120 meV) is $\sim 17\%$ with respect to the 700 meV average value, which is approximately the same order of magnitude as the error among the predictions of GGA+ U , SCAN, and SCAN+ U , highlighting the normal magnitude of errors that can be expected across theory and experiments for electrodes. On the other hand, GGA does underestimate the

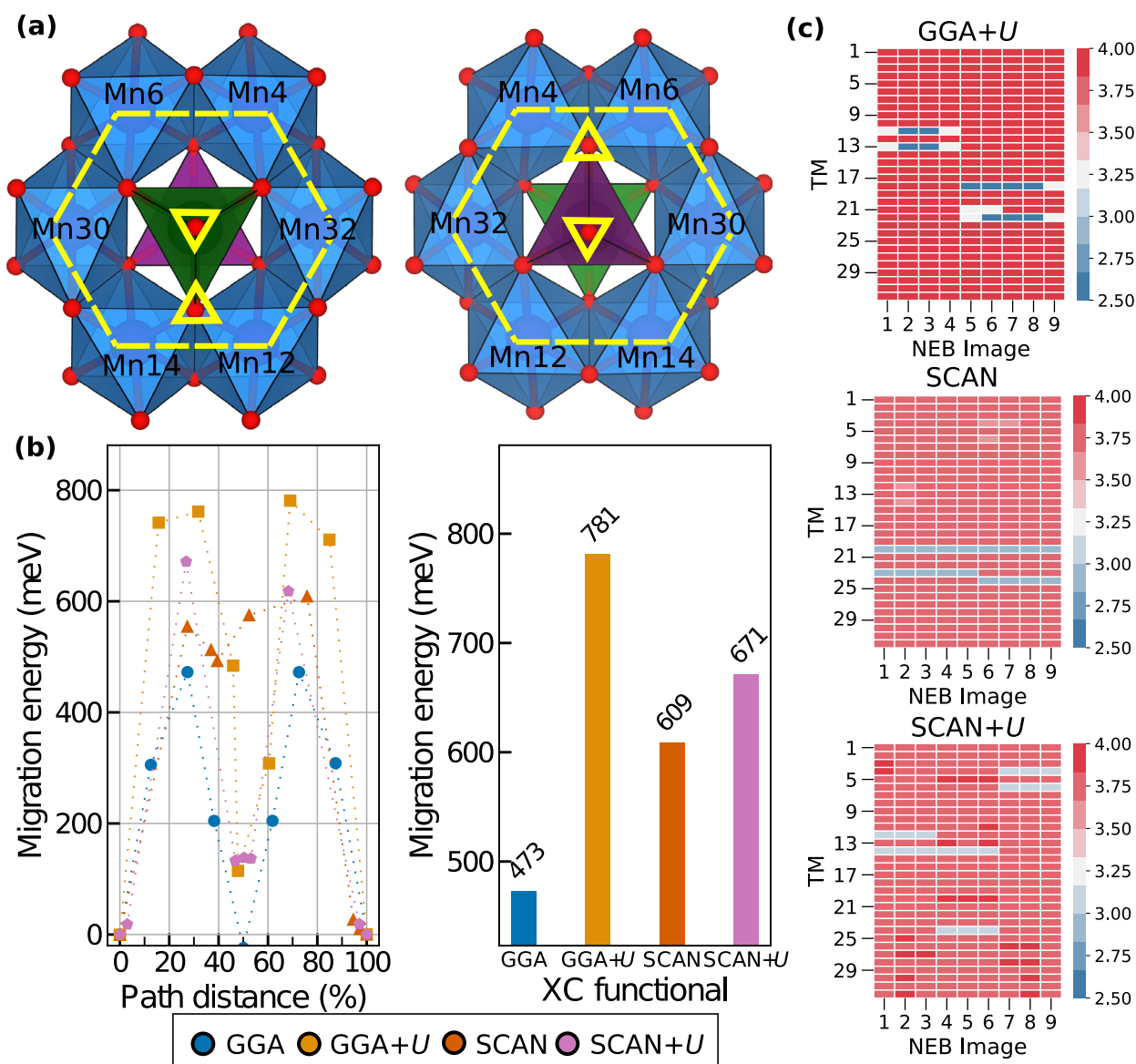


Fig. 5 Migration barriers computed for spinel- MgMn_2O_4 . **a** Top and bottom views of the Mn "ring" sites (dashed yellow lines) adjacent to the intermediate 16c site during Mg migration. The initial and the final Mg ions are represented by the green and purple tetrahedra, respectively. The yellow triangles represent additional Mn sites (see text for further description). **b** MEPs and E_m . **c** On-site magnetic moments of Mn ions in the MgMn_2O_4 structure as a function of image numbers (i.e., as Mg is undergoing migration), where 1st and 9th images correspond to the initial and final Mg sites, respectively. The number indicated on the TM sites in (c) is identical to the number indicated in text labels for Mn sites in (b).

experimental E_m significantly by $\sim 32\%$. Thus, the addition of the U correction increases the numerical accuracy significantly in the case of GGA, while it does not make a drastic difference in the case of SCAN for MgMn_2O_4 . The smaller difference between SCAN and SCAN+ U E_m predictions, as compared to GGA and GGA+ U , can be due to the better description of XC interactions and lower SIEs in SCAN.

Similar to other materials considered in this work, SCAN does predict a higher E_m than GGA. However, SCAN+ U 's barrier is lower than GGA+ U 's, which may be attributed to the higher magnitude of U correction used in GGA+ U (3.9 eV⁶⁰) as compared to SCAN+ U (2.7 eV⁴⁰). All four XC functionals predict changes of on-site magnetic moments on Mn atoms as the Mg^{2+} migrates, indicating a concurrent migration of electrons resulting in a polaronic hop that is characteristic of semiconducting/insulating electrodes⁵³. The expected behavior is that as the Mg^{2+} ion hops from the initial to the final 8a site (i.e., as image number increases in Fig. 5c),

the oxidation state of the Mn ions closer to the initial 8a site will increase from +3 to +4 (corresponding to a decrease in their magnetic moments), and the vice-versa for Mn ions that are closer to the final 8a site.

Importantly, we find that changes of magnetic moments (and hence electron hopping) are more accurately captured by SCAN, SCAN+ U , and GGA+ U than plain GGA, as indicated by two distinct Mn atoms displaying lower magnetic moments (i.e., Mn^{4+} oxidation state), corresponding to the Mg-vacancy migrating, throughout the NEB. For instance, in SCAN+ U , the holes (Mn^{4+}) are located on Mn12 and Mn14 sites that are closer to the final Mg site (purple tetrahedron in Fig. 5a) at the beginning of Mg migration (i.e., holes are closer to the vacancy). Subsequently, as Mg migrates to its final position, the holes also migrate to Mn4 and Mn6 sites that are closer to the initial Mg site (green tetrahedron). Thus, SCAN+ U captures the hole (electron) hop that occurs alongside the Mg hop. In the case of SCAN, Mn20 tends to

have its magnetic moment constant throughout the NEB as the Mn20 octahedron shares its vertex with both the initial and the final positions of the Mg tetrahedron, and hence accommodates the hole (Mn^{4+}) better as the Mg-vacancy migrates. Mn24, which is closer to the initial $8a$, has its magnetic moment decreased as Mg moves from image 1 to 9 in the SCAN-NEB calculation, while the opposite behavior is observed in the case of Mn23, which is closer to the final $8a$.

Layered-LiCoO₂

The diffusion of Li ions in layered-LiCoO₂ during the charging and discharging process occurs across each Li layer. The two possible Li migration pathways are: (i) the tetrahedral site hop (TSH) or divacancy hop, and (ii) the oxygen dumbbell hop (ODH) or monovacancy hop, as illustrated in panels a and b of Fig. 6,

respectively⁷². Hollow black rectangles in Fig. 6 represent Li vacancies in the octahedrally coordinated Li layers. The arrows correspond to the migration path of the Li-ion, specifically, via the intermediate tetrahedral site in the TSH mechanism and passing through an O–O bond in ODH. Previous studies have shown that Li ions prefer the TSH mechanism, involving the presence of an additional Li-vacancy adjacent to the migration pathway (hence termed DV hop) instead of the ODH mechanism, which can be attributed to electrostatic repulsions of the migrating Li with other Li and Co cations^{71,72}.

While Fig. 6c plots the MEPs and E_m associated with the DV hop, the data for ODH is provided in Supplementary Fig. 1. The MEP of the DV hop shows a local minima corresponding to the intermediate tetrahedral site for all functionals, and the calculated E_m are lower than the monovacancy hop, as expected. The experimental barrier for LiCoO₂ is ~300 meV, as observed in NMR

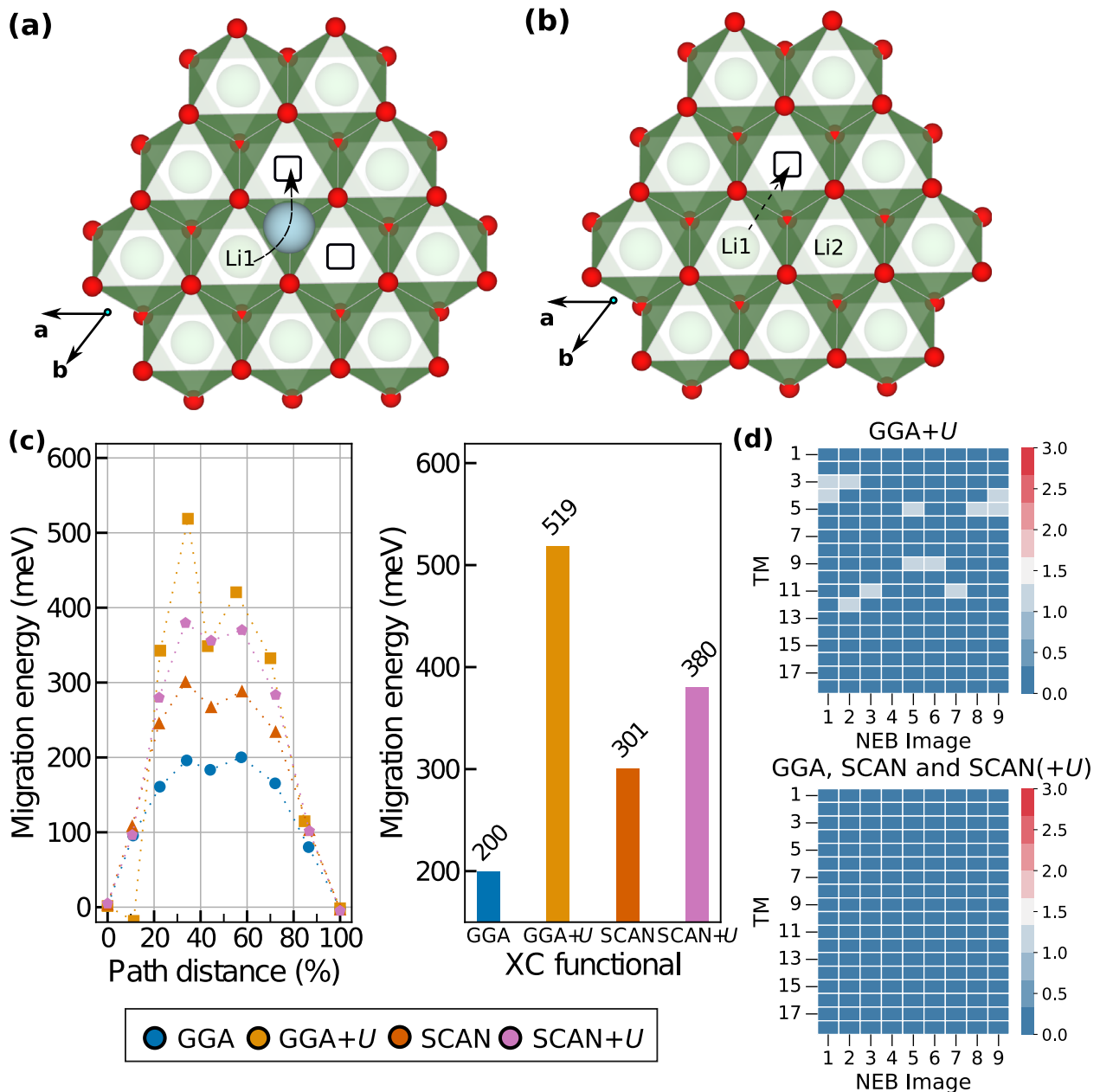


Fig. 6 MEPs and the corresponding barriers for LiCoO₂. **a, b** display the divacancy and monovacancy Li migration mechanisms, respectively, in LiCoO₂. **c** Calculated MEPs and E_m . **d** On-site magnetic moment changes of the Co ions as a function of Li-ion migration with the GGA+U (top panel) and GGA/SCAN/SCAN+U functionals (bottom panel).

studies of Nakamura et al.⁷⁸. Notably, SCAN predicts a barrier that is identical to the experimental value, while GGA underestimates the barrier by ~33%. Both GGA+*U* and SCAN+*U* overestimate E_m versus experiment, by ~73% and 26%, respectively. However, the qualitative trends remain identical across all the XC functionals. Note that due to convergence difficulties, we performed the SCAN+*U*-NEB calculation using relaxed SCAN-NEB structures (see Section S1 of ESI for details).

Figure 6d displays the on-site magnetic moments of the TM (i.e., Co) ions in the LiCoO₂ supercell as a function of the image number. The magnitude of the heat map ranges from 0 to 3 μ_B , where lower (higher) values indicate Co³⁺ (Co⁴⁺). Unlike MgMn₂O₄, only GGA+*U* tends to capture a local electron hop, as indicated by changes in magnetic moments across several Co ions as Li migrates, whereas the other functionals exhibit negligible changes in magnetic moments. Note that Li_{*x*}CoO₂ is a metallic compound over a large range of Li concentrations⁷¹, which indicates that the magnetic moments of Co ions should not change significantly as Li migrates (due to electron delocalization in a metal). This aspect is captured well by all functionals except GGA+*U*, even though all four functionals predict semiconducting behavior in pristine-LiCoO₂, without any Li-vacancy⁴⁵. Thus, the large error in the GGA+*U*-calculated E_m (versus experiment) can be attributed to the spurious localization of electrons by GGA+*U* in a metallic structure.

DISCUSSION

Given that good mobility of the intercalating cation in electrode and solid electrolyte structures and a proper computational framework for estimating ionic mobility with reasonable accuracy is essential for developing high-energy-density battery systems, we analyze the accuracy of a few commonly employed XC approximations within DFT in predicting E_m in battery materials. Specifically, we benchmark predictions of GGA, SCAN, GGA+*U*, and SCAN+*U* XC frameworks for six distinct electrodes, and consider GGA and SCAN (with and without NELECT/CI) for three typical solid electrolytes. Importantly, we observe that SCAN has better numerical accuracy in estimating E_m across the structures considered than other XC frameworks. Additionally, we observe that the difference in E_m predicted by SCAN and SCAN+*U* (MAE across electrodes is ~51 meV) is consistently lower than the difference in E_m predicted by GGA and GGA+*U* (MAE ~200.5 meV). Thus, for E_m predictions, we do not expect the addition of *U* to make a significant difference with SCAN. This behavior can be attributed to overall lower SIEs in SCAN than GGA. The addition of NELECT or CI does not affect the qualitative or the quantitative nature of the barrier in the case of GGA or SCAN in solid electrolytes (except in Li₃PO₄).

In electrodes, GGA+*U*, SCAN, and SCAN+*U* XC frameworks capture changes of on-site magnetic moments, which quantify the extent of electron hopping that occurs in conjunction with an ionic hop, better compared to GGA, in the case of semiconducting MgMn₂O₄. However, in the case of metallic Li_{*x*}CoO₂, we find GGA, SCAN, and SCAN+*U* to be better than GGA+*U*. Thus, the specific choice of the XC functional, especially between GGA and GGA+*U*, will depend on the electrode's electronic nature, while we expect the addition of *U* (or not) to make a less significant impact on E_m calculations with SCAN, irrespective of the underlying electronic structure.

Given that *U* is a “tunable” parameter in GGA+*U* and SCAN+*U* calculations, it is important to examine the effect of changing the *U* magnitude in both XC functionals in predicting E_m . We have calculated the E_m for LiMn₂O₄ with GGA+*U* and SCAN+*U*, where the *U* values are 2.7 and 3.9 eV, respectively, with the results plotted in Supplementary Fig. 5 of the ESI. Note that the *U* values optimized for oxidation enthalpies for Mn-oxides are 3.9 and 2.7 eV with GGA+*U* and SCAN+*U*, respectively^{40,60}. Thus, we vary

the *U* magnitude by ~1 eV, which is usually sufficient to observe qualitative differences in predictions. Furthermore, we observe that the *U* value, derived by from linear-response theory⁴⁷, for MnO (averaged over its rocksalt and zinc blende polymorphs) with SCAN+*U* is 2.8 eV⁹⁸, which is similar to the optimized *U* used in this work. For GGA+*U*, the value derived with linear-response (3.2 eV) is within the range of *U* values (2.7–3.9 eV) explored for LiMn₂O₄ in this study⁹⁸.

On one hand, we find that changing the *U* value does not change the E_m predictions with GGA+*U* (349–364 meV, see Supplementary Figs. 4, 5), with values at *U* = 2.7 and 3.9 eV in reasonable agreement with experiment (~500 meV, Table 1)⁷⁹. On the other hand, SCAN+*U* predictions of E_m vary significantly with varying *U* (327–750 meV), with the SCAN+*U* = 2.7 E_m (327 meV) in better agreement with experiment. The GGA+*U* = 3.9 and SCAN+*U* = 2.7 NEB calculations capture better changes of the on-site magnetic moment of the Mn sites as the Li⁺ migrates in LiMn₂O₄ (see Supplementary Fig. 5). Thus, we can conclude that SCAN+*U*'s E_m predictions are more sensitive to changes in *U* values compared to GGA+*U*. We expect the *U* values optimized for oxidation enthalpies to describe better the underlying electronic structure with both XC approximations.

Apart from SCAN-calculated E_m being higher than GGA-calculated E_m in general, SCAN overestimates the experimental E_m in select materials, such as MgSc₂Se₄, while GGA underestimates the experimental value in such materials. Thus, we can consider GGA and SCAN to provide qualitative upper and lower bounds to the experimental E_m , which will be an useful exercise to quantify uncertainty in materials where experimental measurements of E_m can be challenging (such as, decoupling grain boundary contributions or other coupled interactions in impedance spectroscopy measurements). To improve such uncertainty quantifications within computational frameworks, E_m calculations using hybrid functionals, especially in electrodes⁹⁹ can also be attempted. Indeed, Barnes et al.⁹⁹ demonstrated that a full NEB optimization using hybrid functionals^{100,101} classified the active and inactive Mg migration pathways in α -MoO₃ better than PBE, albeit at a significantly higher computational cost. Another theoretical framework that may yield accurate E_m predictions is DFT+*U*+*V*, with an additionally tunable “*V*” parameter that represents inter-site electronic interactions¹⁰². Given that experimental errors can be in the ~10% range, any theoretical calculation in a similar ballpark (10–15% error range) can be considered acceptable.

We observe that SCAN has a relatively lower MAE (versus experiments) compared to other XC functionals in E_m predictions. However, to decide if SCAN-based NEBs are worth pursuing, considering the marginal gain in MAE, an examination of the computational cost associated with SCAN calculations is necessary. Figure 7 shows the computational time (in minutes) per image in an NEB calculation normalized to the number of cores used per image, and relative to the time taken in a GGA-NEB calculation (which sets the zero on the y-axis). Note that the objective of our computational time comparison is not to rigorously benchmark the performance of DFT codes, but to get a qualitative idea of the relative cost associated with the different XC functionals considered.

In general, we find that the computational cost for SCAN (red bars) and SCAN+*U* (purple bars) are higher than both GGA (blue) and GGA+*U* (orange) in electrodes, while SCAN appears consistently more expensive than GGA in solid electrolytes (except the 1(d) → 2(c) hop in Li₃PO₄). However, SCAN does exhibit “similar” computational time as GGA (or GGA+*U*) in select materials, including, LiMn₂O₄, Mg_{*x*}Ti₂S₄, MgSc₂Se₄, and Li₃PO₄ (2(c) → 3(d) hop). Nevertheless, both SCAN and SCAN+*U* suffer from convergence difficulties, in addition to increased computational time, especially in electrodes, namely LiCoO₂, LiFePO₄, and NaV₂O₄ (see Section S1 of ESI). Shifting to other meta-GGA

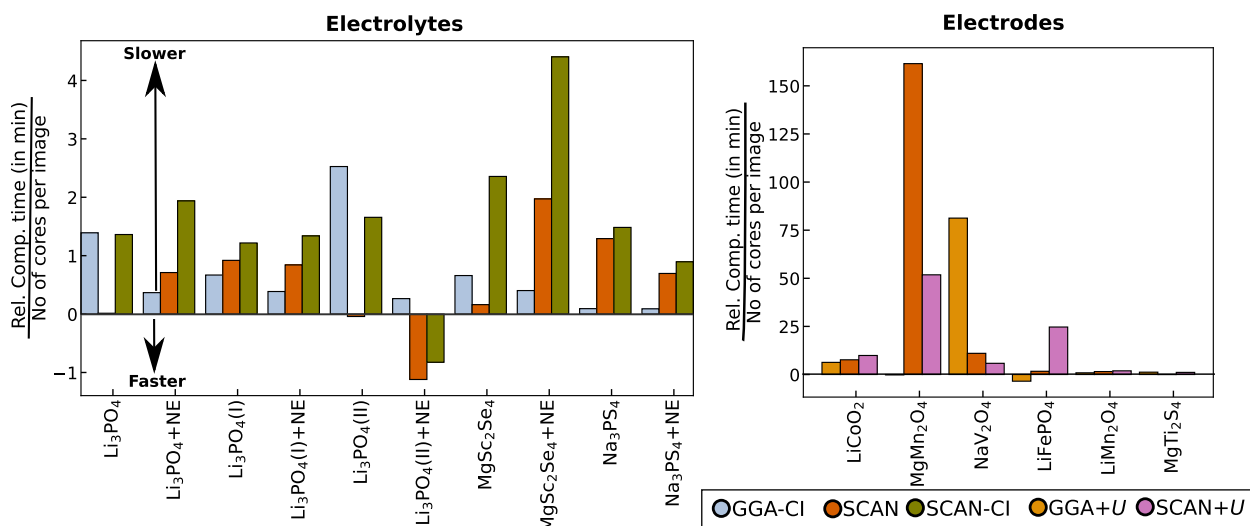


Fig. 7 Relative computing time, in units of minutes taken per number of cores used per NEB image for all the E_m calculations performed in this work. NE and CI represent addition of NELECT and CI, respectively. $\text{Li}_3\text{PO}_4(\text{I})$ and $\text{Li}_3\text{PO}_4(\text{II})$ represent $2(\text{c}) \rightarrow 3(\text{d})$ and $1(\text{d}) \rightarrow 2(\text{c})$ hop respectively.

frameworks, such as the recently developed $r^2\text{SCAN}^{103}$, (which improves convergence while retaining SCAN's numerical accuracy) or the Minnesota functionals³⁶ can be one possible solution to mitigate convergence issues, but rigorous testing is needed. Given the higher computational costs and convergence difficulties of SCAN, GGA may yet be relevant for obtaining “quick” and reasonably accurate E_m predictions. Indeed, GGA may even be more accurate than SCAN in some materials, as illustrated by $\text{Mg}_x\text{Ti}_2\text{S}_4$, MgSc_2Se_4 , and Li_3PO_4 in our work.

In conclusion, we have systematically investigated the accuracy of XC frameworks, namely, GGA, GGA+ U , SCAN, and SCAN+ U in the prediction of migration barriers against existing experimental data for six different electrodes and three different solid electrolytes, spanning diversified crystal systems, to select the appropriate XC candidate for a given structure. Our results indicated that SCAN has better numerical accuracy, on average, than GGA and other Hubbard U -corrected XC frameworks, but with higher computational costs and convergence difficulties. The addition of a uniform background charge or the implementation of the climbing image, in the case of solid electrolytes did not significantly affect the E_m predictions of both GGA and SCAN (except for Li_3PO_4). Also, we found the addition of U corrections to have a lower impact on E_m predictions with SCAN than GGA, which can be attributed to a better description of the electronic exchange contribution by SCAN. However, we also observed that changing U values within the SCAN+ U framework led to more dramatic changes in calculated E_m in LiMn_2O_4 , highlighting the sensitivity of E_m on the U value used in the SCAN+ U description. Thus, we find that all considered functionals are equally reliable (or unreliable) for a systematically accurate prediction of E_m . However, on average, the SCAN functional turns out to provide the most accurate results among the considered functionals, albeit with several exceptions where GGA-based E_m predictions are more accurate than SCAN. Note that if qualitative trends in E_m are essential and the tolerance towards numerical accuracy (versus experiments) is low, GGA remains a highly useful option for all materials. In cases where experimental E_m measurements can be difficult, we observed that GGA- and SCAN-predicted E_m can be used as qualitative lower and upper bounds for the experimental E_m , since predictions of SCAN- E_m are typically larger than GGA. Given that ionic mobility predictions are critical in identifying candidate electrode and solid electrolyte materials for developing high-energy-density battery systems with robust rate performance,

our work will help choose the appropriate XC framework for predicting E_m in materials.

METHODS

Structure relaxations

All DFT calculations were performed using the Vienna ab initio simulation package (VASP 6.1.2) that employs the projector augmented wave (PAW) approximation to describe the effects of core electrons in the many-body wavefunctions^{104–106}. The plane wave basis kinetic energy cutoff was set to 520 eV. A fully automatic, Γ -centered grid generation scheme was used to sample the 1st Brillouin zone, at a density of at least 48 k -points per \AA for relaxing the bulk structures. For NEB calculations, we reduced the k -mesh density 32 per \AA . The input structures for all systems were obtained from the inorganic crystal structure database (ICSD)¹⁰⁷. The lattice vectors, cell volume, and ionic positions of all input bulk structures were relaxed until the total energy and atomic forces were below 0.01 meV and [0.03] eV per \AA , respectively. The U values for GGA+ U calculations used were identical to the ones used in Materials Project⁶⁰. We used the U parameters by Gautam et al.^{40,45} for SCAN+ U calculations.

NEB calculations

To estimate E_m , the fully relaxed endpoint geometries were obtained, and the MEP was initialized by linearly interpolating both the atomic positions and lattice vectors to create seven images between the endpoints, with a spring force constant of 5 eV per \AA between images. The limited-memory Broyden-Fletcher-Goldfarb-Shanno (L-BFGS) method¹⁰⁸ was used to converge to the MEP. The intermediate images were optimized along the reaction coordinate until the total energy converged to within 0.01 meV for each image. The NEB was considered converged if the force component perpendicular to the elastic band was below [0.05] eV per \AA . The barriers were calculated in the dilute-vacancy limit for all the systems, i.e., one Li/Na/Mg vacancy was created in the corresponding supercell with stoichiometric composition^{51,61,75,109}, with the exception of $\text{Mg}_x\text{Ti}_2\text{S}_4$. Appropriate supercells of the corresponding primitive cells were used to avoid spurious interaction between the diffusing species by ensuring that the moving ion was always at a distance $>8 \text{\AA}$ from its periodic image⁸⁵. All E_m calculated in this work correspond to vacancy-mediated mechanisms and are not interstitial-based.

All calculated migration energy profiles are provided either as part of the main text or in the ESI. The structures for which we experienced severe convergence difficulties in our NEB calculations and the strategies we used to overcome such problems are also detailed in the ESI. For E_m calculations with UBC in solid electrolytes, we added the number of valence electrons corresponding to the migrating vacancy to the remaining number of valence electrons contributed by the rest of the atoms in the supercell. In VASP the number of electrons is controlled by the keyword “NELECT”,

which initializes the total valence charge as a “jellium”-background. For example, our NELECT keyword for a migrating Li vacancy in a Li_3PO_4 supercell was Σ (valence electrons of remaining Li, P, and O in supercell) + 1. The number of valence electrons for each atom was determined by the corresponding PAW potential employed in the NEB calculation.

DATA AVAILABILITY

All the computational data presented in this study are freely available to all on our GitHub repository (<https://github.com/sai-mat-group/migration-barriers-project-public>).

CODE AVAILABILITY

All density functional theory calculations in this work were performed using the VASP code (version 6.1.2), which is a licensed software package.

Received: 31 January 2022; Accepted: 22 June 2022;

Published online: 22 July 2022

REFERENCES

- Thackeray, M. M., Wolverton, C. & Isaacs, E. D. Electrical energy storage for transportation—approaching the limits of, and going beyond, lithium-ion batteries. *Energy Environ. Sci.* **5**, 7854–7863 (2012).
- Whittingham, M. S. Introduction: batteries. *Chem. Rev.* **114**, 11413 (2014).
- Vehicle Technologies Office: Advanced battery development, system analysis, and testing. <https://www.energy.gov/eere/vehicles/advanced-battery-development-system-analysis-and-testing> (accessed on April 12, 2014).
- Tomaszewska, A. et al. Lithium-ion battery fast charging: a review. *Transp. J.* **1**, 100011 (2019).
- Li, C. et al. An advance review of solid-state battery: challenges, progress and prospects. *Sustain. Mater. Technol.* **29**, e00297 (2021).
- Aurbach, D. et al. Prototype systems for rechargeable magnesium batteries. *Nature* **407**, 724–727 (2000).
- Canepa, P. et al. Odyssey of multivalent cathode materials: open questions and future challenges. *Chem. Rev.* **117**, 4287–4341 (2017).
- Shterenberg, I., Salama, M., Gofer, Y., Levi, E. & Aurbach, D. The challenge of developing rechargeable magnesium batteries. *MRS Bull.* **39**, 453–460 (2014).
- Orikasa, Y. et al. High energy density rechargeable magnesium battery using earth-abundant and non-toxic elements. *Sci. Rep.* **4**, 1–6 (2014).
- Liu, Q., Wang, H., Jiang, C. & Tang, Y. Multi-ion strategies towards emerging rechargeable batteries with high performance. *Energy Storage Mater.* **23**, 566–586 (2019).
- Liang, Y., Dong, H., Aurbach, D. & Yao, Y. Current status and future directions of multivalent metal-ion batteries. *Nat. Energy* **5**, 646–656 (2020).
- O'Donnell, L. F. & Greenbaum, S. G. Review of multivalent metal ion transport in inorganic and solid polymer electrolytes. *Batteries* **7**, 3 (2021).
- Van der Ven, A., Deng, Z., Banerjee, S. & Ong, S. P. Rechargeable alkali-ion battery materials: theory and computation. *Chem. Rev.* **120**, 6977–7019 (2020).
- Hohenberg, P. & Kohn, W. Inhomogeneous electron gas. *Phys. Rev.* **136**, B864 (1964).
- Kohn, W. & Sham, L. J. Self-consistent equations including exchange and correlation effects. *Phys. Rev.* **140**, A1133 (1965).
- Henkelman, G., Uberuaga, B. P. & Jónsson, H. A climbing image nudged elastic band method for finding saddle points and minimum energy paths. *J. Chem. Phys.* **113**, 9901–9904 (2000).
- Frenkel, D. & Smit, B. *Understanding Molecular Simulation: from Algorithms to Applications*, vol. 1 (Elsevier, 2001).
- He, X., Zhu, Y., Epstein, A. & Mo, Y. Statistical variances of diffusional properties from ab initio molecular dynamics simulations. *npj Comput. Mater.* **4**, 1–9 (2018).
- Gao, Y., Mishra, T. P., Canepa, P. & Sai Gautam, G. Design and characterization of host-frameworks for facile magnesium transport. *Annu. Rev. Mater. Res.* **52**, 6.1–6.30 (2022).
- Perdew, J. P., Burke, K. & Ernzerhof, M. Generalized gradient approximation made simple. *Phys. Rev. Lett.* **77**, 3865 (1996).
- Mantina, M., Wang, Y., Chen, L. Q., Liu, Z. K. & Wolverton, C. First principles impurity diffusion coefficients. *Acta Mater.* **57**, 4102–4108 (2009).
- Bhattacharya, J. & Van der Ven, A. First-principles study of competing mechanisms of nondilute Li diffusion in spinel $\text{Li}_x\text{Ti}_5\text{S}_2$. *Phys. Rev. B* **83**, 144302 (2011).
- Jadidi, Z., Chen, T., Xiao, P., Urban, A. & Ceder, G. Effect of fluorination and Li-excess on the Li migration barrier in Mn-based cathode materials. *J. Mater. Chem. A* **8**, 19965–19974 (2020).
- Koettgen, J., Bartel, C. J. & Ceder, G. Computational investigation of chalcogenide spinel conductors for all-solid-state Mg batteries. *Chem. Commun.* **56**, 1952–1955 (2020).
- Chevrier, V. L., Ong, S. P., Armiento, R., Chan, M. K. Y. & Ceder, G. Hybrid density functional calculations of redox potentials and formation energies of transition metal compounds. *Phys. Rev. B* **82**, 75122 (2010).
- Perdew, J. P., McMullen, E. R. & Zunger, A. Density-functional theory of the correlation energy in atoms and ions: a simple analytic model and a challenge. *Phys. Rev. A* **23**, 2785 (1981).
- Patton, D. C., Porezag, D. V. & Pederson, M. R. Simplified generalized-gradient approximation and anharmonicity: benchmark calculations on molecules. *Phys. Rev. B* **55**, 7454 (1997).
- Hammer, B., Hansen, L. B. & Nørskov, J. K. Improved adsorption energetics within density-functional theory using revised Perdew-Burke-Ernzerhof functionals. *Phys. Rev. B* **59**, 7413 (1999).
- Liu, H.-R., Xiang, H. & Gong, X. G. First principles study of adsorption of O_2 on Al surface with hybrid functionals. *J. Chem. Phys.* **135**, 214702 (2011).
- Aykol, M., Kim, S. & Wolverton, C. Van Der Waals interactions in layered lithium cobalt oxides. *J. Phys. Chem. C* **119**, 19053–19058 (2015).
- Tran, F., Kalantari, L., Traoré, B., Rocquefelte, X. & Blaha, P. Nonlocal van Der Waals functionals for solids: choosing an appropriate one. *Phys. Rev. Mater.* **3**, 63602 (2019).
- Zhao, Y. & Truhlar, D. G. Comparative DFT study of van Der Waals complexes: rare-gas dimers, alkaline-earth dimers, zinc dimer, and zinc-rare-gas dimers. *J. Phys. Chem. A* **110**, 5121–5129 (2006).
- Perdew, J. P. et al. Restoring the density-gradient expansion for exchange in solids and surfaces. *Phys. Rev. Lett.* **100**, 136406 (2008).
- Sarmiento-Perez, R., Botti, S. & Marques, M. A. L. Optimized exchange and correlation semilocal functional for the calculation of energies of formation. *J. Chem. Theory Comput.* **11**, 3844–3850 (2015).
- Armiento, R. & Mattsson, A. E. Functional designed to include surface effects in self-consistent density functional theory. *Phys. Rev. B* **72**, 85108 (2005).
- Zhao, Y. & Truhlar, D. G. Applications and validations of the Minnesota density functionals. *Chem. Phys. Lett.* **502**, 1–13 (2011).
- Sun, J., Ruzsinszky, A. & Perdew, J. P. Strongly constrained and appropriately normed semilocal density functional. *Phys. Rev. Lett.* **115**, 36402 (2015).
- Sun, J. et al. Accurate first-principles structures and energies of diversely bonded systems from an efficient density functional. *Nat. Chem.* **8**, 831–836 (2016).
- Car, R. Fixing Jacob's Ladder. *Nat. Chem.* **8**, 820–821 (2016).
- Gautam, G. S. & Carter, E. A. Evaluating transition metal oxides within DFT-SCAN and SCAN+ U frameworks for solar thermochemical applications. *Phys. Rev. Mater.* **2**, 95401 (2018).
- Zhang, Y. et al. Efficient first-principles prediction of solid stability: towards chemical accuracy. *npj Computational Mater.* **4**, 1–6 (2018).
- Zhang, Y., Sun, J., Perdew, J. P. & Wu, X. Comparative first-principles studies of prototypical ferroelectric materials by LDA, GGA, and SCAN Meta-GGA. *Phys. Rev. B* **96**, 35143 (2017).
- Yang, J. H., Kitchaev, D. A. & Ceder, G. Rationalizing accurate structure prediction in the Meta-GGA SCAN functional. *Phys. Rev. B* **100**, 35132 (2019).
- Wang, L., Maxisch, T. & Ceder, G. Oxidation energies of transition metal oxides within the GGA+ U framework. *Phys. Rev. B* **73**, 195107 (2006).
- Long, O. Y., Gautam, G. S. & Carter, E. A. Evaluating optimal U for 3 d transition-metal oxides within the SCAN+ U framework. *Phys. Rev. Mater.* **4**, 45401 (2020).
- Anisimov, V. I., Zaanen, J. & Andersen, O. K. Band theory and mott insulators: Hubbard U instead of Stoner I . *Phys. Rev. B* **44**, 943 (1991).
- Cococcioni, M. & De Gironcoli, S. Linear response approach to the calculation of the effective interaction parameters in the LDA+ U method. *Phys. Rev. B* **71**, 35105 (2005).
- Sa, N. et al. Structural evolution of reversible Mg insertion into a bilayer structure of $\text{V}_2\text{O}_5 \cdot n\text{H}_2\text{O}$ xerogel material. *Chem. Mater.* **28**, 2962–2969 (2016).
- Sai Gautam, G., Canepa, P., Richards, W. D., Malik, R. & Ceder, G. Role of structural H_2O in intercalation electrodes: the case of Mg in nanocrystalline xerogel- V_2O_5 . *Nano Lett.* **16**, 2426–2431 (2016).
- Liu, M. et al. Spinel compounds as multivalent battery cathodes: a systematic evaluation based on Ab initio calculations. *Energy Environ. Sci.* **8**, 964–974 (2015).
- Gautam, G. S. et al. First-principles evaluation of multi-valent cation insertion into orthorhombic V_2O_5 . *Chem. Commun.* **51**, 13619–13622 (2015).
- Luong, H. D., Pham, T. D., Morikawa, Y., Shibutani, Y. & Dinh, V. A. Diffusion mechanism of Na ion–polaron complex in potential cathode materials NaVOPO_4 and VOPO_4 for rechargeable sodium-ion batteries. *Phys. Chem. Chem. Phys.* **20**, 23625–23634 (2018).
- Ong, S. P., Chevrier, V. L. & Ceder, G. Comparison of small polaron migration and phase separation in olivine LiMnPO_4 and LiFePO_4 using hybrid density functional theory. *Phys. Rev. B* **83**, 75112 (2011).

54. Reticcioli, M., Diebold, U., Kresse, G. & Franchini, C. Small polarons in transition metal oxides, 1–39 (Springer International Publishing, 2019).
55. Long, O. Y., Gautam, G. S. & Carter, E. A. Assessing cathode property prediction via exchange-correlation functionals with and without long-range dispersion corrections. *Phys. Chem. Chem. Phys.* **23**, 24726–24737 (2021).
56. Isaacs, E. B., Patel, S. & Wolverton, C. Prediction of Li intercalation voltages in rechargeable battery cathode materials: effects of exchange-correlation functional, van Der Waals interactions, and Hubbard U . *Phys. Rev. Mater.* **4**, 65405 (2020).
57. Chakraborty, A., Dixit, M., Aurbach, D. & Major, D. T. Predicting accurate cathode properties of layered oxide materials using the SCAN Meta-GGA density functional. *npj Comput. Mater.* **4**, 1–9 (2018).
58. Xu, B. & Meng, S. Factors affecting Li mobility in spinel LiMn_2O_4 —a first-principles study by GGA and GGA+ U methods. *J. Power Sources* **195**, 4971–4976 (2010).
59. Moore, G. C., Horton, M. K., Ganose, A. M., Siron, M. & Persson, K. A. High-throughput determination of Hubbard U and Hund J values for transition metal oxides via linear response formalism. <https://arxiv.org/abs/2201.04213> (2022).
60. Jain, A. et al. Commentary: the materials project: a materials genome approach to accelerating materials innovation. *APL Mater.* **1**, 11002 (2013).
61. Rong, Z. et al. Materials design rules for multivalent ion mobility in intercalation structures. *Chem. Mater.* **27**, 6016–6021 (2015).
62. Bölle, F. T. et al. Autonomous discovery of materials for intercalation electrodes. *Batteries Supercaps* **3**, 488–498 (2020).
63. Martin, S. W. Ionic conduction in phosphate glasses. *J. Am. Ceram. Soc.* **74**, 1767–1784 (1991).
64. Wang, B., Chakoumakos, B. C., Sales, B. C., Kwak, B. S. & Bates, J. B. Synthesis, crystal structure, and ionic conductivity of a polycrystalline lithium phosphorus oxynitride with the $\gamma\text{-Li}_3\text{PO}_4$ structure. *J. Solid State Chem.* **115**, 313–323 (1995).
65. Rojas, R. M., De Vidales, J. L. M., Delgado, A. & Sinisterra, J. V. Microstructural and thermal characterization of basic and stoichiometric lithium phosphates, in relation with their catalytic activity. *J. Solid State Chem.* **106**, 237–252 (1993).
66. Huang, H., Wu, H.-H., Wang, X., Huang, B. & Zhang, T.-Y. Enhancing sodium ionic conductivity in tetragonal- Na_3PS_4 by halogen doping: a first principles investigation. *Phys. Chem. Chem. Phys.* **20**, 20525–20533 (2018).
67. Famprikis, T. et al. Insights into the rich polymorphism of the Na^+ ion conductor Na_3PS_4 from the perspective of variable-temperature diffraction and spectroscopy. *Chem. Mater.* **33**, 5652–5667 (2021).
68. Famprikis, T. et al. Under pressure: mechanochemical effects on structure and ion conduction in the sodium-ion solid electrolyte Na_3PS_4 . *J. Am. Chem. Soc.* **142**, 18422–18436 (2020).
69. Bo, S.-H., Wang, Y. & Ceder, G. Structural and Na-ion conduction characteristics of $\text{Na}_3\text{P}_x\text{Se}_{4-x}$. *J. Mater. Chem. A* **4**, 9044–9053 (2016).
70. Delmas, C., Braconnier, J.-J., Maazaz, A. & Hagenmuller, P. Soft chemistry in A_xMO_2 sheet oxides. *Rev. Chim. Miner.* **19**, 343–351 (1982).
71. Van der Ven, A., Aydinol, M. K. & Ceder, G. First-principles evidence for stage ordering in Li_xCoO_2 . *J. Electrochem. Soc.* **145**, 2149 (1998).
72. Van der Ven, A., Ceder, G., Asta, M. & Tapesch, P. D. First-principles theory of ionic diffusion with nondilute carriers. *Phys. Rev. B* **64**, 184307 (2001).
73. Amatuocci, G. G., Tarascon, J. M. & Klein, L. C. CoO_2 , the end member of the Li_xCoO_2 solid solution. *J. Electrochem. Soc.* **143**, 1114 (1996).
74. Padhi, A. K., Nanjundaswamy, K. S. & Goodenough, J. B. Phospho-olivines as positive-electrode materials for rechargeable lithium batteries. *J. Electrochem. Soc.* **144**, 1188 (1997).
75. Gautam, G. S., Canepa, P., Urban, A., Bo, S.-H. & Ceder, G. Influence of inversion on Mg mobility and electrochemistry in spinels. *Chem. Mater.* **29**, 7918–7930 (2017).
76. Bayliss, R. D. et al. Probing Mg migration in spinel oxides. *Chem. Mater.* **32**, 663–670 (2019).
77. Sun, X. et al. A high capacity thiospinel cathode for Mg batteries. *Energy Environ. Sci.* **9**, 2273–2277 (2016).
78. Nakamura, K. et al. On the diffusion of Li^+ defects in LiCoO_2 and LiNiO_2 . *Solid State Ion.* **135**, 143–147 (2000).
79. Verhoeven, V. W. J. et al. Lithium dynamics in LiMn_2O_4 probed directly by two-dimensional Li NMR. *Phys. Rev. Lett.* **86**, 4314 (2001).
80. Schmidt, J. P. et al. Studies on LiFePO_4 as cathode material using impedance spectroscopy. *J. Power Sources* **196**, 5342–5348 (2011).
81. Månsson, M. et al. Na-ion dynamics in Quasi-1D compound NaV_2O_4 . *J. Phys.: Conf. Ser.* **551**, 012035 (2014).
82. Canepa, P. et al. High magnesium mobility in ternary spinel chalcogenides. *Nat. Commun.* **8**, 1–8 (2017).
83. Moon, C. K. et al. Vacancy-driven Na^+ superionic conduction in new Ca-doped Na_3PS_4 for all-solid-state Na-ion batteries. *ACS Energy Lett.* **3**, 2504–2512 (2018).
84. Asai, T. & Kawai, S. NMR study of Li^+ -ion diffusion in the solid solution $\text{Li}_{3-x}(\text{P}_{1-x}\text{Si}_x)\text{O}_4$ with the $\gamma\text{-Li}_3\text{PO}_4$ structure. *Solid State Ion.* **7**, 43–47 (1982).
85. Chen, T., Sai Gautam, G. & Canepa, P. Ionic transport in potential coating materials for Mg batteries. *Chem. Mater.* **31**, 8087–8099 (2019).
86. Bhandari, A. et al. Electronic structure calculations in electrolyte solutions: methods for neutralization of extended charged interfaces. *J. Chem. Phys.* **153**, 124101 (2020).
87. Wang, Y. et al. Design principles for solid-state lithium superionic conductors. *Nat. Mater.* **14**, 1026–1031 (2015).
88. Lin, Y.-Y. et al. Toward design of cation transport in solid-state battery electrolytes: structure-dynamics relationships. *Curr. Opin. Solid State Mater. Sci.* **24**, 100875 (2020).
89. Torres, J. A. G., Jennings, P. C., Hansen, M. H., Boes, J. R. & Bligaard, T. Low-scaling algorithm for nudged elastic band calculations using a surrogate machine learning model. *Phys. Rev. Lett.* **122**, 156001 (2019).
90. Du, Y. A. & Holzwarth, N. A. W. Li ion diffusion mechanisms in the crystalline electrolyte $\gamma\text{-Li}_3\text{PO}_4$. *J. Electrochem. Soc.* **154**, A999 (2007).
91. Ivanov-Shitz, A. K., Kireev, V. V., Mel'nikov, O. K. & Demianets, L. N. Growth and ionic conductivity of $\gamma\text{-Li}_3\text{PO}_4$. *Crystallogr. Rep.* **46**, 864–867 (2001).
92. Chu, I.-H. et al. Room-temperature all-solid-state rechargeable sodium-ion batteries with a Cl-doped Na_3PS_4 superionic conductor. *Sci. Rep.* **6**, 1–10 (2016).
93. Krauskopf, T., Pompe, C., Kraft, M. A. & Zeier, W. G. Influence of lattice dynamics on Na^+ transport in the solid electrolyte $\text{Na}_3\text{PS}_{4-x}\text{Se}_x$. *Chem. Mater.* **29**, 8859–8869 (2017).
94. Dawson, J. A. et al. Toward understanding the different influences of grain boundaries on ion transport in sulfide and oxide solid electrolytes. *Chem. Mater.* **31**, 5296–5304 (2019).
95. Yu, Z. et al. Exceptionally high ionic conductivity in $\text{Na}_3\text{P}_{0.62}\text{As}_{0.38}\text{S}_4$ with improved moisture stability for solid-state sodium-ion batteries. *Adv. Mater.* **29**, 1605561 (2017).
96. Zhu, Z. Design and optimization of alkali superionic conductors for solid-state batteries using first-principles calculations. Ph.D. thesis, (UC San Diego, 2019).
97. Sanjana, N., Biswas, A. & Sinha, A. Crystal structure of magnesium manganate, MgMn_2O_4 . *J. Sci. Ind. Res. B* **19**, 415–419 (1960).
98. Peng, H. & Perdew, J. P. Synergy of van der Waals and self-interaction corrections in transition metal monoxides. *Phys. Rev. B* **96**, 100101 (2017).
99. Barnes, T. A., Wan, L. F., Kent, P. R. C. & Prendergast, D. Hybrid DFT investigation of the energetics of Mg ion diffusion in $\alpha\text{-MoO}_3$. *Phys. Chem. Chem. Phys.* **20**, 24877–24884 (2018).
100. Heyd, J., Scuseria, G. E. & Ernzerhof, M. Hybrid functionals based on a screened Coulomb potential. *J. Chem. Phys.* **118**, 8207–8215 (2003).
101. Perdew, J. P., Ernzerhof, M. & Burke, K. Rationale for mixing exact exchange with density functional approximations. *J. Chem. Phys.* **105**, 9982–9985 (1996).
102. Ricca, C., Timrov, I., Cococcioni, M., Marzari, N. & Aschauer, U. Self-consistent DFT + U + V study of oxygen vacancies in SrTiO_3 . *Phys. Rev. Res.* **2**, 23313 (2020).
103. Furness, J. W., Kaplan, A. D., Ning, J., Perdew, J. P. & Sun, J. Accurate and numerically efficient $r^2\text{SCAN}$ meta-generalized gradient approximation. *J. Phys. Chem. Lett.* **11**, 8208–8215 (2020).
104. Kresse, G. & Hafner, J. Ab initio molecular dynamics for open-shell transition metals. *Phys. Rev. B* **48**, 13115 (1993).
105. Kresse, G. & Furthmüller, J. Efficient iterative schemes for Ab initio total-energy calculations using a plane-wave basis set. *Phys. Rev. B* **54**, 11169 (1996).
106. Kresse, G. & Joubert, D. From ultrasoft pseudopotentials to the projector augmented-wave method. *Phys. Rev. B* **59**, 1758 (1999).
107. Hellenbrandt, M. The inorganic crystal structure database (icsd)-present and future. *Crystallogr. Rev.* **10**, 17–22 (2004).
108. Nocedal, J. Updating Quasi-Newton matrices with limited storage. *Math. Comput.* **35**, 773–782 (1980).
109. Sai Gautam, G. et al. The intercalation phase diagram of Mg in V_2O_5 from first-principles. *Chem. Mater.* **27**, 3733–3742 (2015).

ACKNOWLEDGEMENTS

G.S.G. acknowledges financial support from the Indian Institute of Science (IISc) Seed Grant, SG/MHRD/20/0020 and SR/MHRD/20/0013 and the Science and Engineering Research Board (SERB) of the Department of Science and Technology, Government of India, under sanction number SRG/2021/000201. R.D. thanks the Ministry of Human Resource Development, Government of India, for financial assistance. B.S. and P.C. acknowledge funding from the National Research Foundation under the NRF Fellowship NRF12-2020-0012. P.C. acknowledges support from the Singapore Ministry of Education Academic Fund Tier 1 (R-284-000-186-133). G.S.G. thanks the International Travel Support scheme of SERB, under sanction number ITS/2022/000391, and the Indian Institute of Metals for travel support. R.D. and G.S.G. acknowledge the computational resources provided by the Supercomputer Education and Research Center, IISc, for enabling some of the density functional theory and nudged elastic band calculations showcased in this work. A significant

portion of the computational work of this article was performed on resources of the National Supercomputing Center, Singapore (<https://www.nscg.sg>).

AUTHOR CONTRIBUTIONS

Study was planned by G.S.G. and P.C. Computational data was generated and analyzed by all four authors. R.D., with inputs from B.S., prepared the initial paper draft. P.C. and G.S.G. edited the paper and supervised all aspects of the work. All authors approve of the final version of the paper and are accountable for all aspects of the work.

COMPETING INTERESTS

The authors declare no competing interests.

ADDITIONAL INFORMATION

Supplementary information The online version contains supplementary material available at <https://doi.org/10.1038/s41524-022-00837-0>.

Correspondence and requests for materials should be addressed to Pieremanuele Canepa or Gopalakrishnan Sai Gautam.

Reprints and permission information is available at <http://www.nature.com/reprints>

Publisher's note Springer Nature remains neutral with regard to jurisdictional claims in published maps and institutional affiliations.



Open Access This article is licensed under a Creative Commons Attribution 4.0 International License, which permits use, sharing, adaptation, distribution and reproduction in any medium or format, as long as you give appropriate credit to the original author(s) and the source, provide a link to the Creative Commons license, and indicate if changes were made. The images or other third party material in this article are included in the article's Creative Commons license, unless indicated otherwise in a credit line to the material. If material is not included in the article's Creative Commons license and your intended use is not permitted by statutory regulation or exceeds the permitted use, you will need to obtain permission directly from the copyright holder. To view a copy of this license, visit <http://creativecommons.org/licenses/by/4.0/>.

© The Author(s) 2022